THE JOURNAL OF PHYSICAL CHEMISTRY C

Article

Cite This: J. Phys. Chem. C 2019, 123, 19412−19420

pubs.acs.org/JPCC

# Comparison of Thermomechanical Properties for Weaved Polyethylene and Its Nanocomposite Based on the CNT Junction by Molecular Dynamics Simulation

Bo Zhang, Ji Li, Shan Gao, Wei Liu, and Zhichun Liu*

School of Energy and Power Engineering, Huazhong University of Science and Technology (HUST), Wuhan 430074, China

Supporting Information

**ABSTRACT:** Improving the thermomechanical performance of polymers can efficiently enlarge their applications in thermal management. Previous studies have shown that the carbon nanotube junction (CNTJ) possesses robust mechanical and electrical properties. Nevertheless, the application of the CNTJ in polymers still remains an open question. In this work, the thermomechanical properties of weaved polyethylene (PE) and the PE-CNTJ are numerically investigated and compared via molecular dynamics simulation. Heat flux decomposition methods are applied to uncover the contributions from different interactions. The results show that the thermal conductivity of the PE-CNT is 3.83-fold that of weaved PE. The underlying mechanisms are revealed from polymer morphology and phonon perspectives. The effect of temperature on the thermal conductivity of the PE-CNTJ is also investigated. Furthermore, a theoretical model is used to predict the impacts of filler and matrix on the thermal conductivity of the PE-CNTJ. With respect to mechanical properties, the stress−strain simulations show that Young's modulus of the PE-CNTJ is 5.3 times that of weaved PE. This work can deliver new perspectives on designing polymer nanocomposites with both superior thermal and mechanical properties.

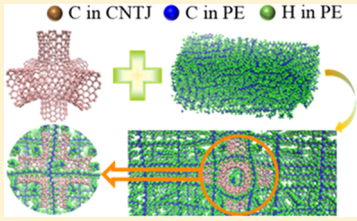


## 1. INTRODUCTION

Polymers have a wide range of applications due to various advantages, including low cost, low mass density, strong corrosion resistance, and easy to process. However, the thermal conductivity of bulk polymers is very low (0.1−0.5 W $m^{-1}$ $K^{-1}$), which extremely limits their applications in thermal management.[1−3] With respect to dielectric materials, phonons play a dominant role in thermal transport. The low thermal conductivity of bulk polymers is mainly attributed to the structural defects including voids, impurity, chaotic chain arrangements, and entanglements among chains, which tremendously hinder phonon transport.[4−6]

Over the past few decades, the thermal transport in polymers attracts great attention and has been extensively studied. On the one hand, the intrinsic thermal conductivity of polymers can vary over a wide range. Henry and Chen discovered that the thermal conductivity of single polyethylene (PE) chains can go beyond 100 W $m^{-1}$ $K^{-1}$ via molecular dynamics (MD) simulation.[7] Lv et al. observed divergent thermal conductivity of single polythiophene (Pth) chains using the sonication method in conjunction with MD simulation.[8] Wang et al. found that the thermal conductivity of single-chain PE can be as high as 1400 W $m^{-1}$ $K^{-1}$ through anharmonic lattice dynamics.[9] Tu et al. found that the thermal conductivity of PE strands can be further enhanced over 100 W $m^{-1}$ $K^{-1}$ under the combination of torsion and tension.[10] Yu et al. found that the thermal conductivity of single chains of epoxy resin can achieve 33.8 W $m^{-1}$ $K^{-1}$ under moderate tension.[11] Meng et al. discovered that the thermal conductivity of crystalline poly(ethylene oxide) (PEO) can be much higher than amorphous PEO.[12] An et al. investigated the effects of cross-linking and water content on the thermomechanical properties of polyacrylamide hydrogels.[13] Zhang et al. discovered that a rigid backbone can efficiently reduce phonon scatterings and facilitate phonon transport in polymers.[14] Luo et al. discovered that a larger spatial extension and stiffer chain backbone can effectively enhance thermal transport along backbones.[15−17]

In addition to simulation, thermally conductive polymers have been fabricated in experiments. Shen et al. fabricated ultradrawn PE nanofibers with a thermal conductivity of up to 104 W $m^{-1}$ $K^{-1}$.[18] Shrestha et al. fabricated crystalline PE nanofibers with high thermal conductivity by a local heating method.[19] Xu et al. fabricated PE films with a thermal conductivity as high as 62 W $m^{-1}$ $K^{-1}$ via flow extrusion and tension.[20] Singh et al. discovered that the thermal conductivity of chain-oriented Pth nanofibers can be 4.4 W $m^{-1}$ $K^{-1}$.[21] Xu et al. prepared thermally conductive poly(3-hexylthiophene) through the bottom-up oxidative chemical vapor deposition method.[22] Cao et al. prepared thermally conductive PE nanowire arrays via a nanoporous template wetting technique.[23] Li et al. prepared various polymer nanofibers like PE and poly(vinyl alcohol) by the electrospinning method.[24,25] Tang et al. found that the thermal conductivity of PAAm hydrogels is strongly associated with the degree of cross-linking.[26]

On the other hand, tuning thermal transport in polymer nanocomposites has made much progress. Liao et al. found that the axial thermal conductivity of aligned carbon

Received: June 18, 2019
Revised: July 16, 2019
Published: July 17, 2019

Downloaded via HUAZHONG UNIV SCIENCE & TECHNOLOGY on September 2, 2019 at 00:54:08 (UTC).
See https://pubs.acs.org/sharingguidelines for options on how to legitimately share published articles.

ACS Publications © 2019 American Chemical Society



DOI: 10.1021/acs.jpcc.9b05794
J. Phys. Chem. C 2019, 123, 19412−19420

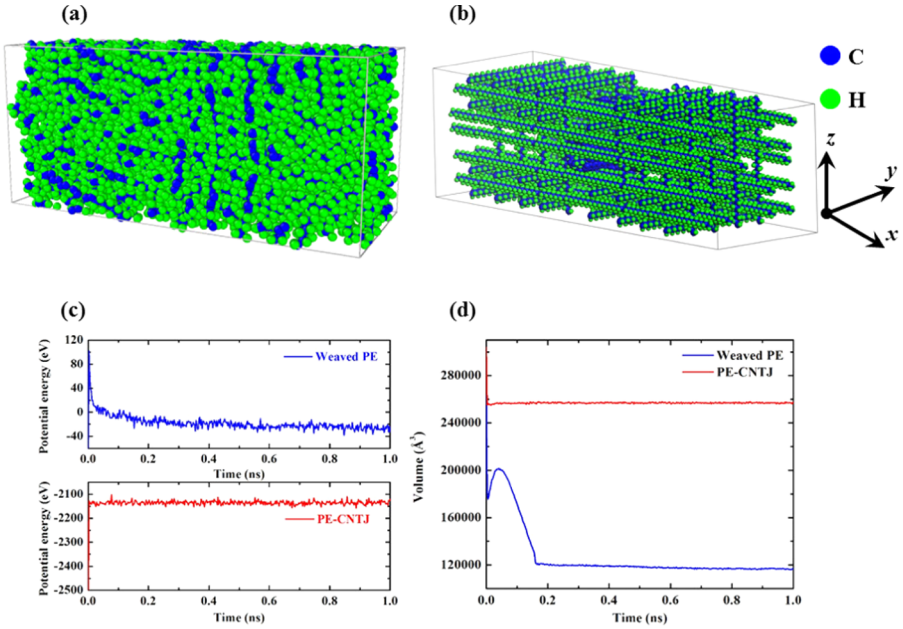


**Figure 1.** Simulation models and relaxation in the NPT ensemble. (a) Weaved PE. (b) PE-CNTJ. (c) Potential energy evolution in the NPT ensemble. (d) Volume evolution in the NPT ensemble.

nanotube−polyethylene nanocomposite can be up to 60 W $m^{-1}$ $K^{-1}$.[27] Pettes et al. found that the thermal conductivity of three-dimensional (3D) foams can be increased to 1.7 W $m^{-1}$ $K^{-1}$ using few-layer graphene.[28] Li et al. found that the thermal conductivity of phase change materials can be increased by 27.7% using 3D porous carbons.[29] Zheng et al. found that the thermal conductivity of polyamide can be increased by five times using multiwalled carbon nanotube (CNT) networks.[30] These studies indicated that the 3D fillers gradually attracted much attention due to high surface areas and isotropic characteristics.

The unfavorable features of nanofibers and membranes like anisotropic thermal conductivity and low mechanical strength impede their applications in industry. Hence, polymers with both high thermal conductivity and modulus are desirable. Carbon nanotube junctions (CNTJs) have been demonstrated to have robust mechanical properties and electrical conductivity.[31−33] However, the applications of CNTJs in polymers have rarely been reported. In this work, we propose to use CNTJs as fillers to improve the thermal and mechanical properties of the PE matrix. The thermomechanical properties of pristine PE and the PE-CNTJ are explored via MD simulations. To further elucidate the difference of thermal transport between PE and the PE-CNTJ, the morphological and phonon characteristics are analyzed.

## 2. METHODOLOGY

All of the MD simulations are performed by employing the Large-scale Atomic/Molecular Massively Parallel Simulator (LAMMPS) package.[34] OVITO and VMD software are chosen to visualize the simulation system.[35,36] Periodic boundary conditions are applied in all three directions. The velocity Verlet algorithm[37] is used to integrate the equation of atomic motion, and the time step is set as 0.25 fs. The initial structure of weaved PE is constructed by aligning PE chains in three directions. To choose the system without size effect, the thermal conductivity of weaved PE with different numbers of atoms (10 223, 12 398, and 12 688) is calculated via nonequilibrium molecular dynamics (NEMD) simulation. The structure details about weaved PE,[38] size effect verification, and sample preparation are shown in Section 2 of the Supporting Information (SI). As shown in Figure S3, the thermal conductivity of weaved PE with more than 10 000 atoms shows no dependence on the number of atoms in the system. The relaxed weaved PE with 12 688 atoms is used in the subsequent thermomechanical simulation, whose size is 86.72 × 34.68 × 38.74 $Å^3$. The PE-CNTJ structure is composed of CNTJ and PE chains. As shown in Figure S4, the CNTJ is connected by six (8, 8) CNTs, whose size is 33 × 33 × 33 $Å^3$. The composition of PE chains in the PE-CNTJ is the same as the weaved PE apart from the number of PE chains in three directions. The overall number of atoms in the PE-CNTJ is 12 674, which is close to the number of atoms in weaved PE. The Tersoff potential[39] and consistent valence force field[40,41] (CVFF) are used to describe the interatomic interactions in the CNTJ and PE, respectively. With respect to the Tersoff potential, the bond energy $U_{ij}$ can be written as

$$U_{ij} = f_c(r_{ij})[f_R(r_{ij}) + b_{ij}f_A(r_{ij})] \tag{1}$$

where $r_{ij}$ represents the distance between atoms $i$ and $j$, $f_c$ is a smooth cutoff function, $b_{ij}$ is the bond-order function, and $f_R$ and $f_A$ stand for the repulsive and attractive potential, respectively. For the CVFF, the total energy $U_{all}$ can be given by

$$U_{all} = \sum_b K_b(r - r_0)^2 + \sum_\theta K_\theta(\theta - \theta_0)^2 + \sum_\varnothing K_\varnothing(1 + d\cos(n\varnothing)) + \sum_{i>j} 4\varepsilon\left[\left(\frac{\sigma}{r_{ij}}\right)^{12} - \left(\frac{\sigma}{r_{ij}}\right)^{6}\right] + \frac{1}{2}\sum_{i=1}^{N}\sum_{j=1,j\neq i}^{N}\frac{q_iq_j}{\varepsilon_0 r_{ij}} \tag{2}$$

where the right terms stand for the bond, angle, dihedral, van der Waals, and Coulombic interactions, respectively. The interactions between the CNTJ and PE are described by the Lennard-Jones (LJ) potential, whose parameters are extracted from the CVFF. The Lorentz−Berthelot mixing rules are used to specify the LJ parameters across different atomic species


DOI: 10.1021/acs.jpcc.9b05794
J. Phys. Chem. C 2019, 123, 19412−19420

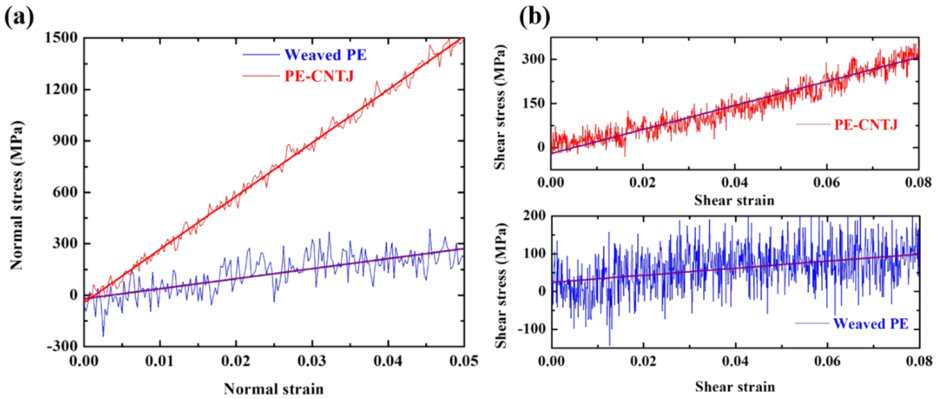


**Figure 2.** Stress−strain relationships of weaved PE and the PE-CNTJ. (a) Normal stress versus normal strain. (b) Shear stress versus shear strain.

(i.e., $\varepsilon_{ij} = \sqrt{\varepsilon_i \varepsilon_j}$, $\sigma_{ij} = (\sigma_i + \sigma_j)/2$). The cutoff distance for the nonbonding interaction is set as 10 Å. The details about potential function are listed in Section 1 of the SI.

The weaved PE and PE-CNTJ first experience energy minimization using a conjugate-gradient algorithm in LAMMPS. The tolerance for energy and force is both set as $10^{-12}$. Then, the two systems continue to relax in the isothermal−isobaric (NPT) ensemble for at least 1 ns. The target temperature and pressure are set as 300 K and 1 atm, respectively. Figure 1a,b displays the relaxed weaved PE and initial PE-CNTJ structure. Figure 1c,d shows that the potential energy and volume of these two systems converge for 1 ns NPT relaxation, which indicates that these two systems reach stable structures. All of the structures are fabricated according to the aforementioned procedure.

After NPT relaxation, these two systems are equilibrated in the canonical ensemble (NVT) for 1 ns, whose temperatures are both controlled at 300 K using Nosé−Hoover thermostats.[42,43] After equilibration, the thin layers (10 Å) at each end of the system are fixed to hinder the heat transfer across the boundary and translational drift of the system.[44] Then, the systems are simulated in the NVE (constant number of atoms, volume, and energy) ensemble. Meanwhile, the 10 Å thick layers next to the fixed layers are used as the heat source (305 K) and heat sink (295 K) with the temperatures being controlled by Langevin thermostats.[45] The systems run 8 ns to fully reach the steady state. The steady-state energy tally and temperature distribution are shown in Section 3 of the SI. The heat flux ($J$) can be calculated from the energy tally ($Q$) recorded on the heat source and sink,[46] which can be written as

$$J = \frac{1}{2S}\left(\left|\frac{dQ_{\text{in}}}{dt}\right| + \left|\frac{dQ_{\text{out}}}{dt}\right|\right) \tag{3}$$

where $S$ is the cross-sectional area. The microscopic expression of the heat flux can be written as[15,47,48]

$$J = \frac{1}{V}\left(\sum_i \boldsymbol{v}_i e_i - \sum_i \mathbf{W}_i \cdot \boldsymbol{v}_i\right) \tag{4}$$

where $\boldsymbol{v}_i$ and $e_i$ are the velocity and local site energy of atom $i$ and $\boldsymbol{W}_i$ denotes the virial stress tensor, which can be written as

$$\begin{aligned}\mathbf{W}_i &= -\frac{1}{2}\sum_{j\neq i} \mathbf{r}_{ij} \otimes \mathbf{F}_{ij} \\ &= -\frac{1}{2}\sum_{j\neq i} \mathbf{r}_{ij} \otimes (\mathbf{F}_{ij}^{\text{bonding}} + \mathbf{F}_{ij}^{\text{nonbonding}})\end{aligned} \tag{5}$$

where $\boldsymbol{F}_{ij}$ is the interatomic force; $\boldsymbol{F}_{ij}^{\text{bonding}}$ and $\boldsymbol{F}_{ij}^{\text{nonbonding}}$ denote the contributions from bonding interaction and nonbonding interaction, respectively. The heat flux can be decomposed into the corresponding convective component, bonding component, and nonbonding component.

$$J(t) = J_{\text{bonding}} + J_{\text{nonbonding}} + J_{\text{conve}} \doteq J_{\text{bonding}} + J_{\text{nonbonding}} \tag{6}$$

With respect to the solids, the convection component of heat flux should be so small that it can be negligible due to zero translational velocity. Hence, we mainly consider the contributions from bonding and nonbonding interactions to thermal transport. The temperature gradient ($\mathrm{d}T/\mathrm{d}x$) can be acquired by fitting the linear temperature distribution away from the thermostats.[47] The thermal conductivity ($\kappa$) can be calculated according to Fourier's law

$$\kappa = \frac{-J}{dT/dx} \tag{7}$$

Similarly, the thermal conductivity can be decomposed into bonding and nonbonding components.[15,16]

$$\kappa \doteq \kappa_{\text{bonding}} + \kappa_{\text{nonbonding}} \tag{8}$$

The final thermal conductivity is averaged over 6 independent simulations with different initial conditions. The details about NEMD simulation are available in Section 3 of the SI.

The stress−strain ($\sigma$−$\varepsilon$) simulations are performed to investigate the mechanical properties of weaved PE and the PE-CNTJ. The simulations about mechanical characteristics are carried out at 300 K. The tensile simulation is carried out in the NPT ensemble along $x$ direction with 1 atm in the lateral directions. The shear deformation is carried out in the NVT ensemble. The strain rate is both set as 0.001/ps and stress is calculated by[49]

$$\sigma_{\alpha\beta} = \frac{1}{V}\left(\sum_{i=1}^{N} m_i \boldsymbol{v}_\alpha^i \boldsymbol{v}_\beta^i + \frac{1}{2}\sum_{i=1}^{N-1}\sum_{j=i+1}^{N} \mathbf{r}_{ij,\alpha}\mathbf{F}_{ij,\beta}\right) \tag{9}$$

where $V$ and $N$ stand for the volume and number of atoms of the system; $\alpha$ and $\beta$ stand for the components of Cartesian coordinate; $m_i$, $\boldsymbol{v}_\alpha^i$, $\boldsymbol{v}_\beta^i$, $\boldsymbol{r}_{ij,\alpha}$, and $\boldsymbol{F}_{ij,\beta}$ stand for the mass of atom


DOI: 10.1021/acs.jpcc.9b05794
J. Phys. Chem. C 2019, 123, 19412−19420

$i$, the $\alpha$-component velocity of atom $i$, the $\beta$-component velocity of atom $i$, the $\alpha$-component relative position between atoms $i$ and $j$, and the $\beta$-component interatomic force between atoms $i$ and $j$, respectively.

## 3. RESULTS AND DISCUSSION

The stress−strain curves are shown in Figure 2. The Young's modulus and shear modulus can be obtained by fitting the corresponding stress−strain curves, which can be given by[50]

$$E = \frac{d\sigma}{d\varepsilon}\Big|_{\varepsilon \to 0} \tag{10}$$

The larger slope on the stress−strain curves indicates that the PE-CNTJ has a higher modulus than weaved PE regardless of Young's modulus or shear modulus. The thermal conductivity of weaved PE and the PE-CNTJ can be calculated via NEMD simulations. The results are shown in Figure 3. The thermal conductivity and Young's modulus of the PE-CNTJ are 3.45 ± 0.25 W m$^{-1}$ K$^{-1}$ and 31.04 GPa, which are three- and fivefold higher than those of the weaved PE (0.9 ± 0.1 W m$^{-1}$ K$^{-1}$ and 5.85 GPa), respectively.

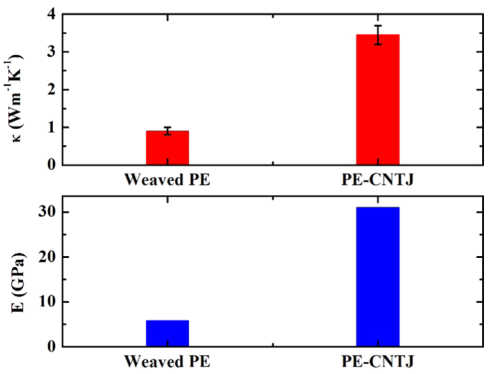


**Figure 3.** Thermal and mechanical properties of weaved PE and the PE-CNTJ.

The heat flux decomposition method is applied to investigate the contributions to thermal transport from different interactions. The results of thermal conductivity decomposition are shown in Figure 4. Obviously, the bonding interaction to thermal transport plays a dominant role in weaved PE and the PE-CNTJ, which conforms to Luo's studies.[15,16] In addition, the bonding interaction contributes more to thermal transport in the PE-CNTJ, which denotes that the morphology of PE-CNTJ facilitates thermal transport along the backbone of the PE chain. Although the numerical value of nonbonding thermal conductivity is close, the proportion of nonbonding contribution to thermal transport is different in weaved PE and the PE-CNTJ. As shown in Figure 4b, the nonbonding interaction still plays a moderate role in thermal transport of weaved PE, whereas the contribution to thermal transport from nonbonding interaction in the PE-CNTJ is less significant.

To elucidate the significant difference between weaved PE and the PE-CNTJ, the morphology analysis and phonon spectrum analysis are conducted. We first conduct the X-ray diffraction (XRD) simulation, which is based on a mesh of reciprocal lattice nodes defined by the entire simulation domain using simulated radiation of wavelength lambda.[11] The sharp peaks in XRD demonstrate that the system has high crystallinity, whereas the broad peaks demonstrate that the system is disordered.[51,52] As shown in Figure 5, the XRD patterns of the PE-CNTJ and PE display sharp peaks, which indicate that the two systems have ordered structure. Compared with weaved PE, the higher intensity in the XRD pattern of the PE-CNTJ indicates that the PE-CNTJ has higher crystallinity than weaved PE.

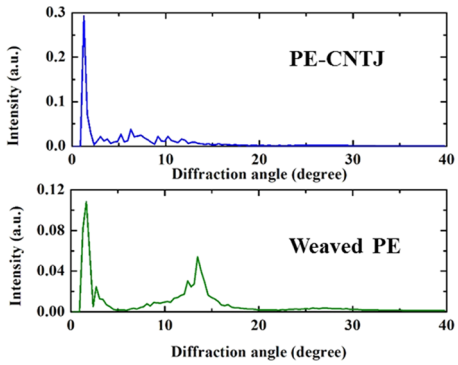


**Figure 5.** XRD patterns of the PE-CNTJ and weaved PE.

The radius of gyration ($R_g$) can indicate the spatial extension of polymer chains, which is defined as[53]

$$R_g^2 = \frac{1}{M}\sum_i m_i(\boldsymbol{r}_i - \boldsymbol{r}_{cm})^2 \tag{11}$$

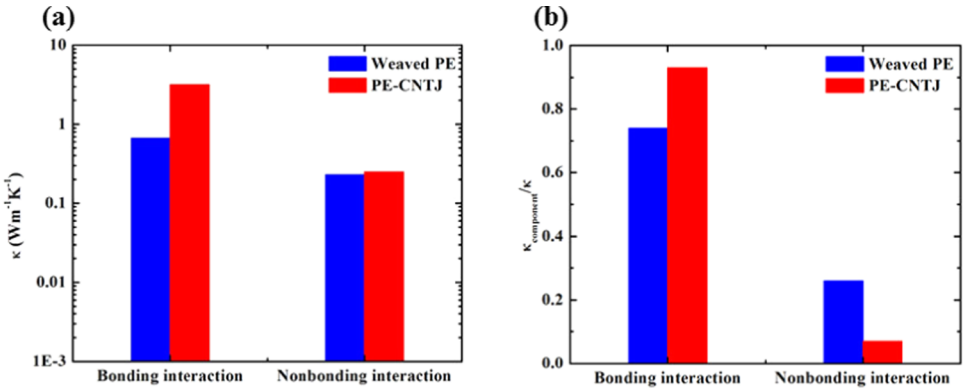


**Figure 4.** (a) Bonding and nonbonding components of thermal conductivity. (b) The proportion of bonding and nonbonding contributions to thermal conductivity.



DOI: 10.1021/acs.jpcc.9b05794
J. Phys. Chem. C 2019, 123, 19412−19420

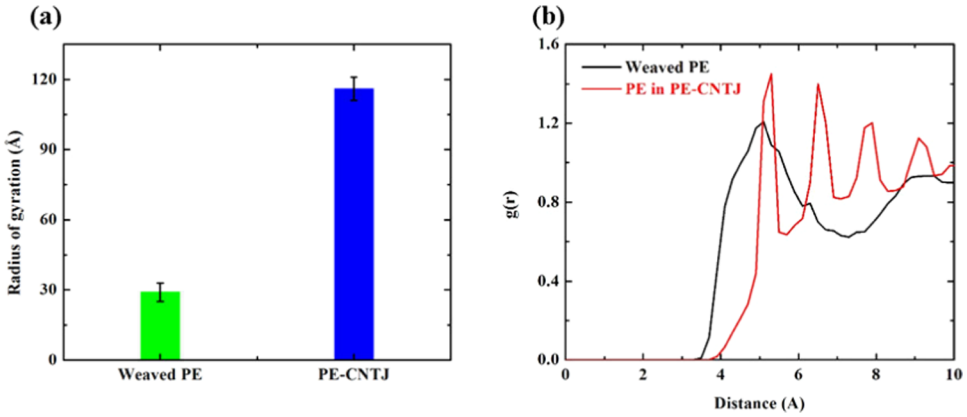


**Figure 6.** (a) Radius of gyration comparison between weaved PE and PE-CNTJ. (b) The RDF comparison between weaved PE and PE-CNTJ.

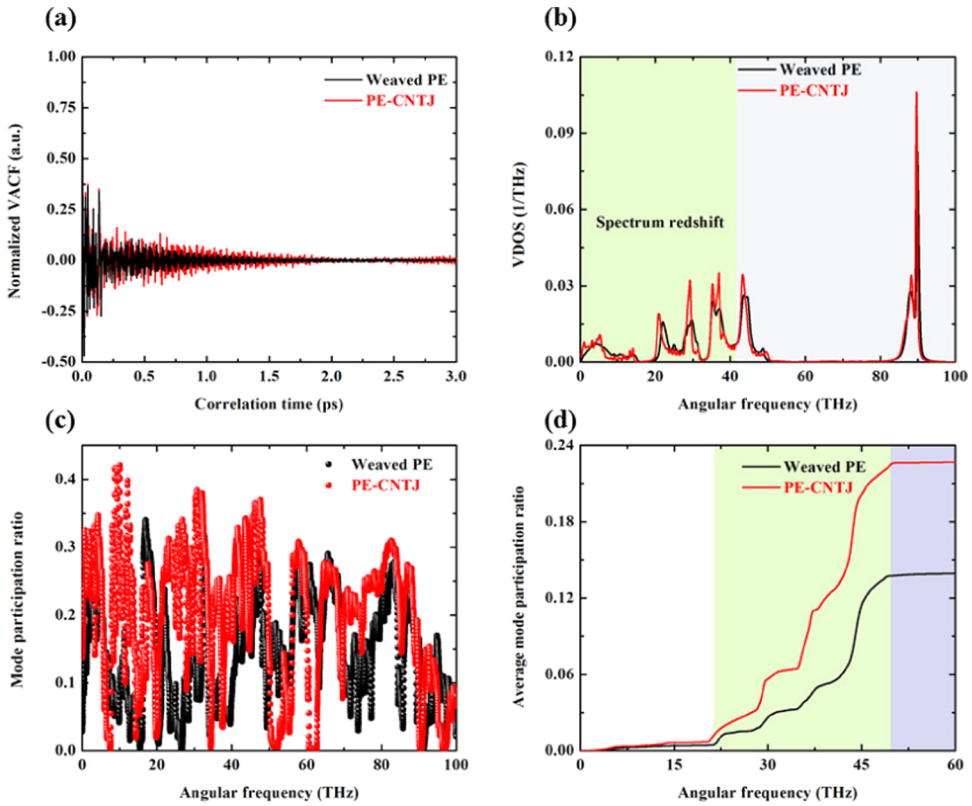


**Figure 7.** (a) Normalized VACF of weaved PE and the PE-CNTJ. (b) VDOS spectra of weaved PE and the PE-CNTJ. (c) MPR spectra of weaved PE and the PE-CNTJ. (d) Average MPR of weaved PE and the PE-CNTJ.

where $M$, $\boldsymbol{r}_i$, and $\boldsymbol{r}_{cm}$ are the total mass, the position of atom $i$, and the center of the group, respectively. The radial distribution function[54] (RDF) can describe the atomic distribution, which can be written as

$$g(r) = \frac{n(r)}{4\pi r^2 \rho \Delta r} \tag{12}$$

where $\rho$ is the atomic number density, $r$ is the distance of reference atoms and neighbor atoms, and $n(r)$ is the number of atoms in a spherical shell with width $\Delta r$. Here, the carbon atoms in the PE chain is chosen as reference atoms and $\Delta r$ is set as 0.2 Å. The cutoff distance for RDF calculation is the same as the cutoff distance of nonbonding interaction. The radius of gyration and RDF diagram of weaved PE and the PE-CNTJ are shown in Figure 6. Figure 6a demonstrates that the PE-CNTJ has a much higher radius of gyration than weaved PE, hence the PE-CNTJ has a larger spatial extension than the weaved PE.[16,51] Figure 6b shows that the RDF of the PE-CNTJ has more distinctive peaks than the weaved PE. Therefore, the PE-CNTJ has a more ordered structure than weaved PE.[27] The ordered structure and large spatial extension can facilitate thermal transport along chain's backbone, which agrees with the results of heat flux decomposition.

Based on the kinetic theory, the thermal conductivity is strongly related to the phonon properties, which can be written as

$$\kappa = \frac{1}{3V}\int_0^{\omega_m} \hbar\omega \frac{\partial f_{BE}}{\partial T} v_g(\omega) v_g(\omega) \tau(\omega) \mathrm{VDOS}(\omega)\, \mathrm{d}\omega \tag{13}$$



DOI: 10.1021/acs.jpcc.9b05794
J. Phys. Chem. C 2019, 123, 19412−19420

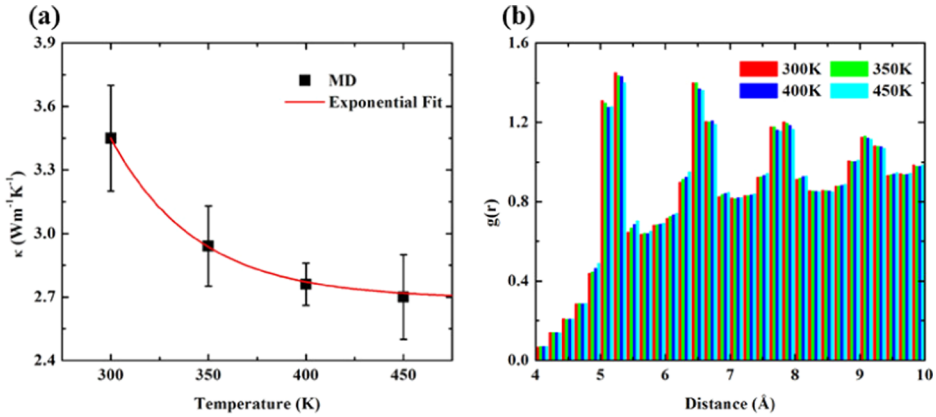


**Figure 8.** (a) Thermal conductivity of the PE-CNTJ as a function of temperature. (b) RDF of the PE-CNTJ at different temperatures.

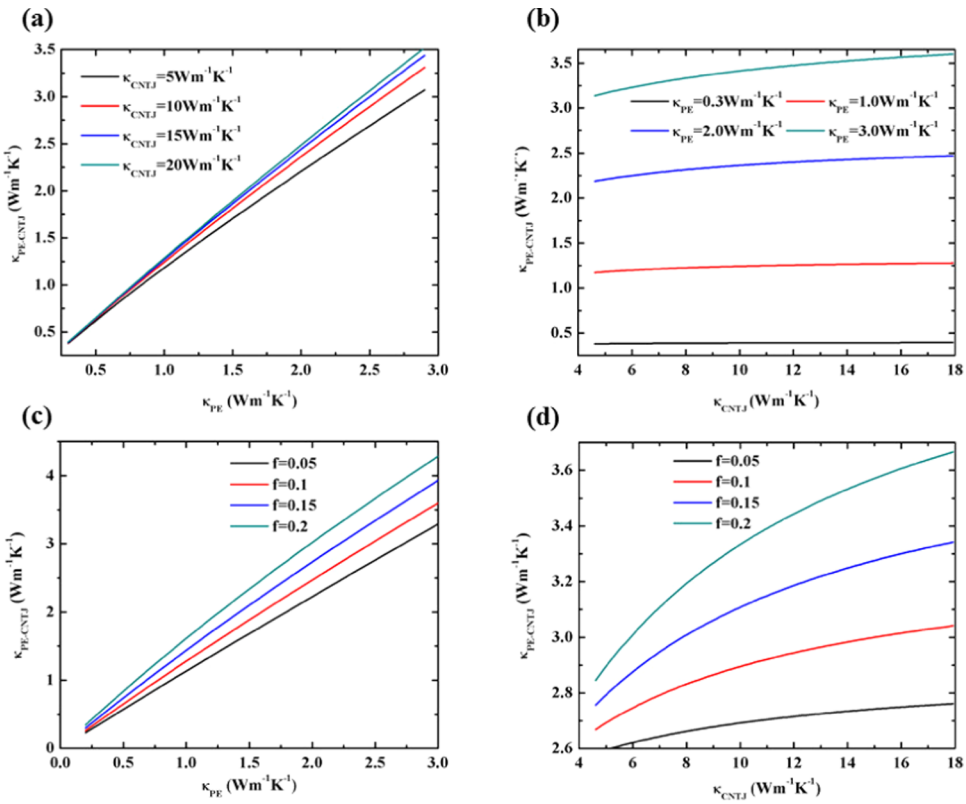


**Figure 9.** (a) Thermal conductivity of the PE-CNTJ varies with the thermal conductivity of PE under different thermal conductivities of the CNTJ. (b) The thermal conductivity of the PE-CNTJ varies with the thermal conductivity of the CNTJ under different thermal conductivities of the PE matrix. (c) The thermal conductivity of the PE-CNTJ varies with the thermal conductivity of the PE matrix under different contents of the CNTJ. (d) The thermal conductivity of the PE-CNTJ varies with the thermal conductivity of the CNTJ under different contents of the CNTJ.

where $\hbar$, $\omega$, $\omega_m$, and $f_{BE}$ are the reduced Planck's constant, angular frequency, cutoff frequency, and Bose−Einstein function; $v_g(\omega)$ and $\tau(\omega)$ are the frequency-dependent group velocity and phonon relaxation time, respectively. VDOS($\omega$) is the vibrational density of states, which determines the frequency distribution of phonons. The VDOS spectra can be obtained via the Fourier transforming velocity autocorrelation function (VACF), which can be written as[55]

$$\mathrm{VDOS}(\omega) = \int_{-\infty}^{+\infty} \frac{\langle \mathbf{v}(0)\cdot\mathbf{v}(t)\rangle}{\langle \mathbf{v}(0)\cdot\mathbf{v}(0)\rangle} \cos(\omega t)\, \mathrm{d}t \tag{14}$$

where $\langle\cdot\rangle$ denotes the ensemble average. Another physical property that can manifest the mode contribution to thermal transport is the mode participation ratio (MPR). The MPR can characterize the proportion of atoms participating in an eigenvibration, which can be defined as[56−58]

$$\mathrm{MPR}(\omega) = \frac{1}{N}\frac{\left(\sum_i \mathrm{VDOS}_i(\omega)^2\right)^2}{\sum_i \mathrm{VDOS}_i(\omega)^4} \tag{15}$$

where the $\mathrm{VDOS}_i$ ($\omega$) is the local VDOS of the ith atom. The overall localization degree can be evaluated by the average MPR, which can be defined as[59]



DOI: 10.1021/acs.jpcc.9b05794
J. Phys. Chem. C 2019, 123, 19412−19420

$$\mathrm{MPR}_{\mathrm{ave}}(\omega) = \int_0^{\omega} \mathrm{MPR}(\omega)\cdot\mathrm{VDOS}(\omega)\,\mathrm{d}\omega / \int_0^{\omega} \mathrm{VDOS}(\omega)\,\mathrm{d}\omega \tag{16}$$

Here, we ignore phonons with high frequency due to their negligible contribution to thermal transport. Figure 7a indicates that the normalized VACF attenuates to zero with oscillation during the correlation time. Figure 7b indicates that the phonon spectra of PE-CNTJ and weaved PE overlap well in the high-frequency region. However, compared with weaved PE, the phonon spectrum of the PE-CNTJ shows a red shift in the low-frequency region. More low-frequency phonons emerge in the phonon spectrum of the PE-CNTJ. With respect to ordered polymers, the low-frequency and moderate-frequency phonons play a dominant role in thermal transport. The MPR spectra shown in Figure 7c,d indicate that the overall MPR of the PE-CNTJ is higher than that of weaved PE, which confirms that the phonon modes of PE-CNTJ are more delocalized than those of weaved PE. Therefore, the VDOS and MPR spectra both demonstrate that the PE-CNTJ has better thermal transport properties than weaved PE.

The effect of temperature on the thermal conductivity of the PE-CNTJ is investigated and displayed in Figure 8a. The exponential fitting is conducted to predict the variation of thermal conductivity versus temperature. The thermal conductivity of PE-CNTJ first decreases and then converges to 2.7 W $m^{-1}$ $K^{-1}$ with the increase of temperature, which is twofold higher than the PE matrix. Based on Matthiessen's rule, the total phonon relaxation time of the system can be given by[60,61]

$$1/\tau = 1/\tau_{\mathrm{T}} + 1/\tau_{\mathrm{s}} \tag{17}$$

where $1/\tau_{\mathrm{T}}$ and $1/\tau_{\mathrm{s}}$ are the temperature- and structure-induced phonon scattering rates, respectively. The anharmonic phonon−phonon scattering rates induced by temperature increase with the increase of temperature, which can result in the decrease of thermal conductivity. The structure-induced phonon scattering rates is intimately related to the structural characteristics.[38] Previous studies have confirmed that the thermal conductivity of polymers is strongly associated with the polymer morphology.[14−16,62] The RDF of the PE-CNTJ at different temperatures is compared in Figure 8b. It can be seen that the peak intensity of the RDF decreases slightly with the increase of temperature. However, the peak position of the RDF changes little with the increase of temperature, which indicates that the structure of the PE-CNTJ is very stable and the morphological change can be negligible.

The Maxwell−Eucken model is employed to predict the variation of thermal conductivity of the PE-CNTJ ($\kappa_{\mathrm{PE\text{-}CNTJ}}$) with filler content $\phi$, filler and matrix thermal conductivity ($\kappa_{\mathrm{CNTJ}}$, $\kappa_{\mathrm{PE}}$), which can be written as[63]

$$\kappa_{\mathrm{PE-CNTJ}} = \kappa_{\mathrm{PE}}\left[\frac{\kappa_{\mathrm{CNTJ}} + 2\kappa_{\mathrm{PE}} + 2\phi(\kappa_{\mathrm{CNTJ}} - \kappa_{\mathrm{PE}})}{\kappa_{\mathrm{CNTJ}} + 2\kappa_{\mathrm{PE}} - 2\phi(\kappa_{\mathrm{CNTJ}} - \kappa_{\mathrm{PE}})}\right] \tag{18}$$

The thermal conductivities of the PE matrix and CNTJ are in the range of 0.3−3.0 and 4.62−20 W $m^{-1}$ $K^{-1}$, respectively.[14,64] The filler content is in the range of 0.05−0.2. The content of the CNTJ is chosen as 0.1 in Figure 9a,b. The thermal conductivity of the CNTJ is chosen as 17.92 W $m^{-1}$ $K^{-1}$ in Figure 9c,[64] and the thermal conductivity of PE is chosen as 2.5 W $m^{-1}$ $K^{-1}$ in Figure 9d. As shown in Figure 9a,b, the thermal conductivity of the composite greatly depends on the thermal conductivity of the matrix at low filler loadings. That means enhancing the intrinsic thermal conductivity of polymers is crucial to increase the thermal conductivity of the composite under low filler contents. Figure 9c,d confirms that increasing the filler content can improve the thermal transport property of the composite. Moreover, the thermal conductivity of the filler grows in importance under high filler loadings.

## 4. CONCLUSIONS

To summarize, we propose a novel PE-CNTJ nanostructure and investigate its thermomechanical properties via NEMD simulations. The simulation results confirm that the thermal conductivity and Young's modulus of the PE-CNTJ are 3.83- and 5.3-fold that of weaved PE, respectively. Compared with weaved PE, the morphology analysis indicates that the PE-CNTJ has more ordered structure and larger spatial extension. The phonon spectra comparison demonstrates that more low-frequency phonon modes emerge in the phonon spectra of the PE-CNTJ. The mode participation ratio spectra comparison indicates that the phonon modes of the PE-CNTJ are more delocalized. The characteristics of morphology and phonon spectra confirm that phonons can be transported more efficiently in the PE-CNTJ. Furthermore, the PE-CNTJ still maintains a satisfying thermal conductivity even at high temperature. Under low filler loadings, the Maxwell−Eucken model shows that the intrinsic thermal conductivity of the matrix plays a decisive role in the thermal conductivity of the composite. Our work can provide useful guidance for designing polymer nanocomposites with both superior thermal and mechanical properties.

## ■ ASSOCIATED CONTENT

### Supporting Information

The Supporting Information is available free of charge on the ACS Publications website at DOI: 10.1021/acs.jpcc.9b05794.

Potential function; size effect verification and sample preparation; nonequilibrium molecular dynamics simulation. (PDF)

## ■ AUTHOR INFORMATION


### Corresponding Author

*E-mail: zcliu@hust.edu.cn. Tel: 86-27-87542618.

### ORCID

Zhichun Liu: 0000-0001-9645-3052


### Notes

The authors declare no competing financial interest.

## ■ ACKNOWLEDGMENTS

The authors are grateful to Xiaoxiang Yu, Quanwen Liao, Ping Zhou, Peng Mao, Meng An, and Nuo Yang for useful discussions. This work was supported by the National Natural Science Foundation of China (Grant no. 51776079) and the National Key Research and Development Program of China (No. 2017YFB0603501-3). The work was carried out at the National Supercomputer Center in Tianjin, and the calculations were performed on TianHe-1(A).

## ■ REFERENCES


(1) Mark, J. E. *Physical Properties of Polymer Handbook*; Springer, 2007; Vol. *1076*, pp 93−339.

(2) Chen, H.; Ginzburg, V. V.; Yang, J.; Yang, Y.; Liu, W.; Huang, Y.; Du, L.; Chen, B. Thermal Conductivity of Polymer-Based




DOI: 10.1021/acs.jpcc.9b05794
J. Phys. Chem. C 2019, 123, 19412−19420

Composites: Fundamentals and Applications. *Prog. Polym. Sci.* **2016**, *59*, 41−85.
(3) Han, Z.; Fina, A. Thermal Conductivity of Carbon Nanotubes and Their Polymer Nanocomposites: A Review. *Prog. Polym. Sci..* **2011**, *36*, 914−944.
(4) Huang, C.; Qian, X.; Yang, R. Thermal Conductivity of Polymers and Polymer Nanocomposites. *Mater. Sci. Eng., R* **2018**, *132*, 1−22.
(5) Xu, X.; Chen, J.; Zhou, J.; Li, B. Thermal Conductivity of Polymers and Their Nanocomposites. *Adv. Mater.* **2018**, *30*, No. 1705544.
(6) Guo, J.; Dong, L.; Xi, Q.; Li, Y.; Xu, X.; Zhou, J.; Nakayama, T.; Liang, Z.; Chen, D.; Li, B. Dimensional Crossover of Heat Conduction in Amorphous Polyimide Nanofibers. *NatI. Sci. Rev.* **2018**, *5*, 500−506.
(7) Henry, A.; Chen, G. High Thermal Conductivity of Single Polyethylene Chains Using Molecular Dynamics Simulations. *Phys. Rev. Lett.* **2008**, *101*, No. 235502.
(8) Lv, W.; Winters, R. M.; DeAngelis, F.; Weinberg, G.; Henry, A. Understanding Divergent Thermal Conductivity in Single Polythiophene Chains Using Green−Kubo Modal Analysis and Sonification. *J. Phys. Chem. A* **2017**, *121*, 5586−5596.
(9) Wang, X.; Kaviany, M.; Huang, B. Phonon Coupling and Transport in Individual Polyethylene Chains: A Comparison Study with the Bulk Crystal. *Nanoscale* **2017**, *9*, 18022−18031.
(10) Tu, R.; Liao, Q.; Zeng, L.; Liu, Z.; Liu, W. Impact of Torsion and Stretching on the Thermal Conductivity of Polyethylene Strands. *Appl. Phys. Lett.* **2017**, *110*, No. 101905.
(11) Li, S.; Yu, X.; Bao, H.; Yang, N. High Thermal Conductivity of Bulk Epoxy Resin by Bottom-up Parallel-Linking and Strain: A Molecular Dynamics Study. *J. Phys. Chem. C* **2018**, *122*, 13140−13147.
(12) Meng, H.; Yu, X.; Feng, H.; Xue, Z.; Yang, N. Superior Thermal Conductivity of Poly (Ethylene Oxide) for Solid-State Electrolytes: A Molecular Dynamics Study. *Int. J. Heat Mass Transfer* **2019**, *137*, 1241−1246.
(13) An, M.; Demir, B.; Wan, X.; Meng, H.; Yang, N.; Walsh, T. R. Predictions of Thermo-Mechanical Properties of Cross-Linked Polyacrylamide Hydrogels Using Molecular Simulations. *Adv. Theory Simul.* **2019**, *2*, No. 1800153.
(14) Zhang, T.; Wu, X.; Luo, T. Polymer Nanofibers with Outstanding Thermal Conductivity and Thermal Stability: Fundamental Linkage between Molecular Characteristics and Macroscopic Thermal Properties. *J. Phys. Chem. C* **2014**, *118*, 21148−21159.
(15) Wei, X.; Zhang, T.; Luo, T. Chain Conformation-Dependent Thermal Conductivity of Amorphous Polymer Blends: The Impact of Inter- and Intra-Chain Interactions. *Phys. Chem. Chem. Phys.* **2016**, *18*, 32146−32154.
(16) Zhang, T.; Luo, T. Role of Chain Morphology and Stiffness in Thermal Conductivity of Amorphous Polymers. *J. Phys. Chem. B* **2016**, *120*, 803−812.
(17) Zhang, T.; Luo, T. High-Contrast, Reversible Thermal Conductivity Regulation Utilizing the Phase Transition of Polyethylene Nanofibers. *ACS Nano* **2013**, *7*, 7592−7600.
(18) Shen, S.; Henry, A.; Tong, J.; Zheng, R.; Chen, G. Polyethylene Nanofibres with Very High Thermal Conductivities. *Nat. Nanotechnol.* **2010**, *5*, 251.
(19) Shrestha, R.; Li, P.; Chatterjee, B.; Zheng, T.; Wu, X.; Liu, Z.; Luo, T.; Choi, S.; Hippalgaonkar, K.; de Boer, M. P.; Shen, S. Crystalline Polymer Nanofibers with Ultra-High Strength and Thermal Conductivity. *Nat. Commun.* **2018**, *9*, No. 1664.
(20) Xu, Y.; Kraemer, D.; Song, B.; Jiang, Z.; Zhou, J.; Loomis, J.; Wang, J.; Li, M.; Ghasemi, H.; Huang, X.; Li, X.; Chen, G. Nanostructured Polymer Films with Metal-Like Thermal Conductivity. *Nat. Commun.* **2019**, *10*, No. 1771.
(21) Singh, V.; Bougher, T. L.; Weathers, A.; Cai, Y.; Bi, K.; Pettes, M. T.; McMenamin, S. A.; Lv, W.; Resler, D. P.; Gattuso, T. R.; et al. High Thermal Conductivity of Chain-Oriented Amorphous Polythiophene. *Nat. Nanotechnol.* **2014**, *9*, 384.
(22) Xu, Y.; Wang, X.; Zhou, J.; Song, B.; Jiang, Z.; Lee, E. M. Y.; Huberman, S.; Gleason, K. K.; Chen, G. Molecular Engineered Conjugated Polymer with High Thermal Conductivity. *Sci. Adv.* **2018**, *4*, No. eaar3031.
(23) Cao, B.-Y.; Li, Y.-W.; Kong, J.; Chen, H.; Xu, Y.; Yung, K.-L.; Cai, A. High Thermal Conductivity of Polyethylene Nanowire Arrays Fabricated by an Improved Nanoporous Template Wetting Technique. *Polymer* **2011**, *52*, 1711−1715.
(24) Ma, J.; Zhang, Q.; Mayo, A.; Ni, Z.; Yi, H.; Chen, Y.; Mu, R.; Bellan, L. M.; Li, D. Thermal Conductivity of Electrospun Polyethylene Nanofibers. *Nanoscale* **2015**, *7*, 16899−16908.
(25) Zhang, Y.; Zhang, X.; Yang, L.; Zhang, Q.; Fitzgerald, M. L.; Ueda, A.; Chen, Y.; Mu, R.; Li, D.; Bellan, L. M. Thermal Transport in Electrospun Vinyl Polymer Nanofibers: Effects of Molecular Weight and Side Groups. *Soft Matter* **2018**, *14*, 9534−9541.
(26) Tang, N.; Peng, Z.; Guo, R.; An, M.; Chen, X.; Li, X.; Yang, N.; Zang, J. Thermal Transport in Soft Paam Hydrogels. *Polymers* **2017**, *9*, No. 688.
(27) Liao, Q.; Liu, Z.; Liu, W.; Deng, C.; Yang, N. Extremely High Thermal Conductivity of Aligned Carbon Nanotube-Polyethylene Composites. *Sci. Rep.* **2015**, *5*, No. 16543.
(28) Pettes, M. T.; Ji, H.; Ruoff, R. S.; Shi, L. Thermal Transport in Three-Dimensional Foam Architectures of Few-Layer Graphene and Ultrathin Graphite. *Nano Lett.* **2012**, *12*, 2959−2964.
(29) Li, A.; Dong, C.; Dong, W.; Atinafu, D. G.; Gao, H.; Chen, X.; Wang, G. Hierarchical 3d Reduced Graphene Porous-Carbon-Based Pcms for Superior Thermal Energy Storage Performance. *ACS Appl. Mater. Interfaces* **2018**, *10*, 32093−32101.
(30) Zheng, Y.; Wang, R.; Dong, X.; Wu, L.; Zhang, X. High Strength Conductive Polyamide 6 Nanocomposites Reinforced by Prebuilt Three-Dimensional Carbon Nanotube Networks. *ACS Appl. Mater. Interfaces* **2018**, *10*, 28103−28111.
(31) Mackay, A. L.; Terrones, H. Diamond from Graphite. *Nature* **1991**, *352*, No. 762.
(32) Romo-Herrera, J. M.; Terrones, M.; Terrones, H.; Dag, S.; Meunier, V. Covalent 2d and 3d Networks from 1d Nanostructures: Designing New Materials. *Nano Lett.* **2007**, *7*, 570−576.
(33) Yao, Y.; Fu, K. K.; Zhu, S.; Dai, J.; Wang, Y.; Pastel, G.; Chen, Y.; Li, T.; Wang, C.; Li, T.; Hu, L. Carbon Welding by Ultrafast Joule Heating. *Nano Lett.* **2016**, *16*, 7282−7289.
(34) Plimpton, S. Fast Parallel Algorithms for Short-Range Molecular Dynamics. *J. Comput. Phys.* **1995**, *117*, 1−19.
(35) Stukowski, A. Visualization and Analysis of Atomistic Simulation Data with Ovito−the Open Visualization Tool. *Modell. Simul. Mater. Sci. Eng.* **2009**, *18*, No. 015012.
(36) Humphrey, W.; Dalke, A.; Schulten, K. Vmd: Visual Molecular Dynamics. *J. Mol. Graphics* **1996**, *14*, 33−38.
(37) Swope, W. C.; Andersen, H. C.; Berens, P. H.; Wilson, K. R. A Computer Simulation Method for the Calculation of Equilibrium Constants for the Formation of Physical Clusters of Molecules: Application to Small Water Clusters. *J. Chem. Phys.* **1982**, *76*, 637−649.
(38) Luo, D.; Huang, C.; Huang, Z. Decreased Thermal Conductivity of Polyethylene Chain Influenced by Short Chain Branching. *J. Heat Transfer* **2018**, *140*, No. 031302.
(39) Kınacı, A.; Haskins, J. B.; Sevik, C.; Çağın, T. Thermal Conductivity of Bn-C Nanostructures. *Phys. Rev. B* **2012**, *86*, No. 115410.
(40) Dauber-Osguthorpe, P.; Roberts, V. A.; Osguthorpe, D. J.; Wolff, J.; Genest, M.; Hagler, A. T. Structure and Energetics of Ligand Binding to Proteins: Escherichia Coli Dihydrofolate Reductase-Trimethoprim, a Drug-Receptor System. *Proteins* **1988**, *4*, 31−47.
(41) Maple, J. R.; Dinur, U.; Hagler, A. T. Derivation of Force Fields for Molecular Mechanics and Dynamics from Ab Initio Energy Surfaces. *Proc. Natl. Acad. Sci. U.S.A.* **1988**, *85*, 5350−5354.
(42) Nosé, S. A Unified Formulation of the Constant Temperature Molecular Dynamics Methods. *J. Chem. Phys.* **1984**, *81*, 511−519.
(43) Hoover, W. G. Canonical Dynamics: Equilibrium Phase-Space Distributions. *Phys. Rev. A* **1985**, *31*, 1695−1697.


DOI: 10.1021/acs.jpcc.9b05794
J. Phys. Chem. C 2019, 123, 19412−19420

(44) Ma, R.; Wan, X.; Zhang, T.; Yang, N.; Luo, T. Role of Molecular Polarity in Thermal Transport of Boron Nitride−Organic Molecule Composites. *ACS Omega* **2018**, *3*, 12530−12534.
(45) Tang, C.-J.; Yu, X.-X.; Li, G.; Yang, N.; Lü, J.-T. Phonon Thermal Transport Properties of Graphene Periodically Embedded with Four- and Eight-Membered Rings: A Molecular Dynamics Study. *ES Mater. Manuf.* **2019**, *3*, 16−21.
(46) Wei, X.; Luo, T. Role of Ionization in Thermal Transport of Solid Polyelectrolytes. *J. Phys. Chem. C* **2019**, *123*, 12659−12665.
(47) Yang, N.; Zhang, G.; Li, B. Violation of Fourier's Law and Anomalous Heat Diffusion in Silicon Nanowires. *Nano Today* **2010**, *5*, 85−90.
(48) Fan, Z.; Pereira, L. F. C.; Wang, H.-Q.; Zheng, J.-C.; Donadio, D.; Harju, A. Force and Heat Current Formulas for Many-Body Potentials in Molecular Dynamics Simulations with Applications to Thermal Conductivity Calculations. *Phys. Rev. B* **2015**, *92*, No. 094301.
(49) Liu, T.-H.; Pao, C.-W.; Chang, C.-C. Effects of Dislocation Densities and Distributions on Graphene Grain Boundary Failure Strengths from Atomistic Simulations. *Carbon* **2012**, *50*, 3465−3472.
(50) Liu, T.-H.; Pao, C.-W.; Chang, C.-C. Thermal Response of Grain Boundaries in Graphene Sheets under Shear Strain from Atomistic Simulations. *Comput. Mater. Sci.* **2013**, *70*, 163−170.
(51) Ma, H.; Tian, Z. Effects of Polymer Topology and Morphology on Thermal Transport: A Molecular Dynamics Study of Bottlebrush Polymers. *Appl. Phys. Lett.* **2017**, *110*, No. 091903.
(52) Ma, H.; Tian, Z. Significantly High Thermal Rectification in an Asymmetric Polymer Molecule Driven by Diffusive Versus Ballistic Transport. *Nano Lett.* **2018**, *18*, 43−48.
(53) Ma, H.; Tian, Z. Effects of Polymer Chain Confinement on Thermal Conductivity of Ultrathin Amorphous Polystyrene Films. *Appl. Phys. Lett.* **2015**, *107*, No. 073111.
(54) Haile, J. M.; Johnston, I.; Mallinckrodt, A. J.; McKay, S. Molecular Dynamics Simulation: Elementary Methods. *Comput. Phys.* **1993**, *7*, 625.
(55) Dickey, J. M.; Paskin, A. Computer Simulation of the Lattice Dynamics of Solids. *Phys. Rev.* **1969**, *188*, 1407−1418.
(56) Loh, G. C.; Teo, E. H. T.; Tay, B. K. Phonon Localization around Vacancies in Graphene Nanoribbons. *Diamond Relat. Mater.* **2012**, *23*, 88−92.
(57) Bao, H.; Chen, J.; Gu, X.; Cao, B. A Review of Simulation Methods in Micro/Nanoscale Heat Conduction. *ES Energy Environ.* **2018**, *1*, 16−55.
(58) Liu, Y.; Cheng, Y.; Hu, R.; Luo, X. Nanoscale Thermal Cloaking by in-Situ Annealing Silicon Membrane. *Phys. Lett. A* **2019**, *383*, 2296−2301.
(59) Chen, J.; Zhang, G.; Li, B. Phonon Coherent Resonance and Its Effect on Thermal Transport in Core-Shell Nanowires. *J. Chem. Phys.* **2011**, *135*, No. 104508.
(60) Ziman, J. M. *Electrons and Phonons: The Theory of Transport Phenomena in Solids*; Oxford University Press, 2001.
(61) Dashora, P.; Gupta, G. On the Temperature Dependence of the Thermal Conductivity of Linear Amorphous Polymers. *Polymer* **1996**, *37*, 231−234.
(62) Zhang, T.; Luo, T. Morphology-Influenced Thermal Conductivity of Polyethylene Single Chains and Crystalline Fibers. *J. Appl. Phys.* **2012**, *112*, No. 094304.
(63) Maxwell, J. C. *A Treatise on Electricity and Magnetism*; Clarendon Press: Oxford, 1873.
(64) Zhang, C.; Akbarzadeh, A.; Kang, W.; Wang, J.; Mirabolghasemi, A. Nano-Architected Metamaterials: Carbon Nanotube-Based Nanotrusses. *Carbon* **2018**, *131*, 38−46.



DOI: 10.1021/acs.jpcc.9b05794
*J. Phys. Chem. C* 2019, 123, 19412−19420